Journal of Radioanalytical and Nuclear Chemistry (2022) 331:469–481
https://doi.org/10.1007/s10967-021-08116-w

Adsorption performance and mechanism of g-C_3N_4/UiO-66 composite for U(VI) from aqueous solution

Jiao Wu[1,2] · Zhouhao Zheng[2] · Kaihao Zhu[2] · Chao Xiang[2] · Jingsong Wang[2] · Jinxiang Liu[2]

Received: 27 August 2021 / Accepted: 15 November 2021 / Published online: 10 January 2022

Abstract

The uranium (VI) adsorption performance of g-C_3N_4/UiO-66 composite (CNUIO) was evaluated under different solution pH values, adsorbent dosages, coexisting ions, contact times, initial U(VI) concentrations, and temperatures. The surface properties and the interaction mechanism between U(VI) and CNUIO were analyzed via SEM–EDS, BET, FT-IR and XPS. CNUIO exhibited the maximum adsorption rate of 95.01% under the conditions of $C_{U(VI)} = 10$ mg/L, pH = 6, M/V = 0.4 g/L, $t = 120$ min, and $T = 298$ K, which was about 25% and 33.73% higher than that of g-C_3N_4 and UiO-66, respectively. The adsorption process was found to be a spontaneous endothermic process and conformed to the pseudo-second-order kinetic model and the Langmuir isothermal adsorption model. SEM–EDS and BET analysis revealed that increasing the specific surface area effectively improved the adsorption capacity of CNUIO. FT-IR spectroscopy and XPS indicated that the removal of U(VI) was attributed to the coordination complexation between the nitrogen-containing and the oxygen-containing functional groups of CNUIO and U(VI). Adsorption–desorption experiment demonstrated that CNUIO has a good reusability.

Keywords Uranium (VI) · Adsorption · Performance · g-C_3N_4/UiO-66 · Mechanism

Introduction

With the rapid development of nuclear energy, huge amounts of uranium-containing water are produced by uranium mining and processing and utilization of uranium raw materials [1]. Untreated uranium-containing water that is directly discharged into aqueous environments can cause serious harm to human health and the ecological environment [2, 3]. Therefore, effective treatment of uranium-containing water has become an urgent environmental concern. Various effective treatment techniques, such as adsorption method, chemical precipitation, ion exchange, redox, and biological treatment [4–7], have been developed, among which the adsorption method is widely used because it is a simple and cost-effective operation.

Graphitic carbon nitride (g-C_3N_4) is a low-cost absorbent that contains both amino and imino groups on its surface [8], and the highly condensed nature of the CN framework endows it with excellent physical and chemical stability [9]. g-C_3N_4 reportedly has a good removal effect on U(VI) [10], Pb (II), Ni (II), Cd (II), and Cu (II) in aqueous solutions [11]. However, the adsorption capacity of g-C_3N_4 is limited because of its small specific surface area owing to its layered structure formed by the stacking of nanosheets and insufficient number of functional groups [12]. To enhance its adsorption capacity, we used morphology control [13] and made a g-C_3N_4 composite with other materials. Liu et al. [14] combined polyaniline with oxidation etching g-C_3N_4. They reported that at the adsorption rate of U(VI) was 36.24% higher than that of g-C_3N_4. A previous study found that $MnFe_2O_4$/PCN composites have an improved adsorption capacity of 182.8 mg/g [15]. Long et al. [16] also found that Fe_3O_4@g-C_3N_4 nano magnetic materials can be used for purifying uranium ion. Wang et al. [17] reported a β-CD modified g-C_3N_4 nanosheet for the extraction of U(VI) with high selectivity from solution system and simulated seawater.

UiO-66, as a zirconium dicarboxylate (Zr)-based metal organic framework material, not only has a large specific

✉ Jinxiang Liu
cafardworm@163.com

[1] Hunan Provincial Key Laboratory of Pollution Control and Resources Technology, School of Civil Engineering, University of South China, Hengyang 421001, China

[2] School of Civil Engineering, University of South China, Hengyang 421001, China

surface area and a high porosity but also has outstanding hydrothermal and chemical stability, which makes it a promising candidate of adsorbent [18]. Luo et al. [19] demonstrated that the maximum adsorption capacity of UiO-66 for U(VI) at pH 5.5 is 109.9 mg/g. Chen et al. [20] found that the uranium adsorption capacity was higher for amine-modified UiO-66. Tripathi et al. [21] prepared a series of functionalized UiO-66 for uranium separation, which exhibit efficient sorption and moderate recyclability to uranium. These works highlight the tremendous potential of UiO-66 in removal of U(VI) from aqueous solution. In order to enhance the adsorption performance of g-C_3N_4, UiO-66 was assembled on its surface to increase its specific surface area and enrich its surface functional groups, which overcame the shortcoming of a single component and improved the capture ability of U (VI). Therefore, in this study, a g-C_3N_4/UiO-66 composite (CNUIO) was synthesized. Its performance in removing U(VI) was evaluated and the underlying mechanism was investigated. This study provides a convenient adsorbent with efficient adsorption performance for the treatment of uranium-containing water.

Experimental section

Materials and chemicals

Melamine, zirconium chloride ($ZrCl_4$), terephthalic acid (H_2BDC), N, N-dimethylformamide (DMF), acetic acid glacial, methanol. Uranium stock solution were prepared from GBW04201 U_3O_8 standard. All reagents were of analytical grade, and all solutions were prepared with deionized water.

Synthesis of g-C_3N_4

Typically, 5 g melamine was placed in a covered crucible and calcined in the muffle furnace at 550 °C for 4 h (2°C/min). After cooling to room temperature and grinding, the obtained yellow powder was g-C_3N_4.

Synthesis of UiO-66

UiO-66 Octahedrons were synthesized by solvothermal method:1.059 g $ZrCl_4$ and 0.755 g H_2BDC were dissolved in 100 ml DMF with a continuous stirring for 1 h and then 60 ml acetic acid glacial was added dropwise to adjust the shape of UiO-66. The solution was transferred into a Teflon-lined stainless steel reactor, followed by being heated at 120 °C for 24 h. The product was washed several times with DMF and methanol. Finally, the UiO-66 samples were obtained after dried in oven at 80 °C overnight.

Synthesis of CNUIO

An improved scheme for preparing CNUIO was adopted herein following the method described in a previous study [22]. First, 1 g of g-C_3N_4 was dispersed into 10 mL DMF and sonicated for 1 h. Then, 0.053 g of $ZrCl_4$ and 0.034 g of H_2BDC were dissolved in 5 mL DMF. Afterward, 6 mL of glacial acetic acid was added dropwise to adjust the shape of UiO-66. The mixture was sonicated at room temperature until the solution became homogeneous. The g-C_3N_4 solution was added into the above solution and continuously ultrasonicated for 1 h. The mixture was transferred into a Teflon-lined stainless steel reactor and then heated at 120 °C for 24 h. The subsequent washing and drying operations were the same those performed on UiO-66. The schematic of the synthesis process is shown in Scheme 1.

Adsorption performance experiments

Uranium stock solution was diluted to the required concentration, and U(VI) adsorption by CNUIO was conducted through batch experiments. First, the pH of 50 mL U(VI)

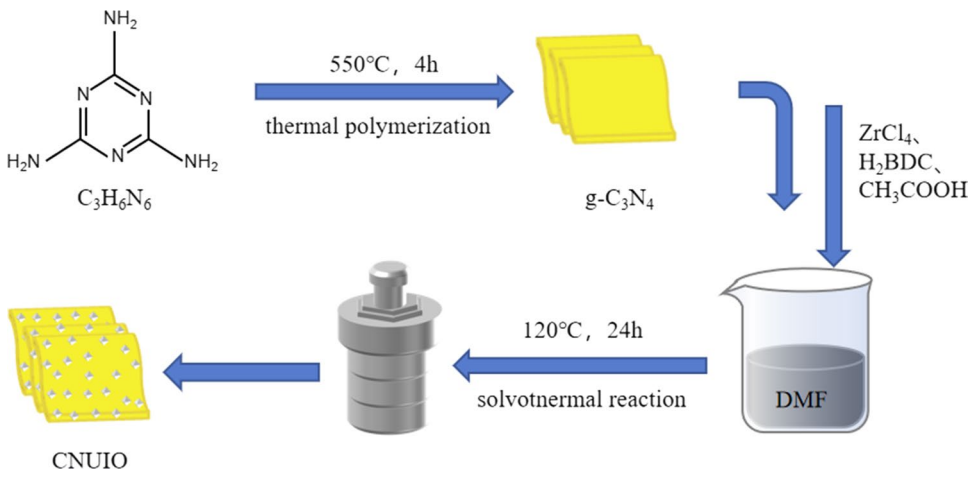

Scheme 1. Schematic illustration for synthesis of the CNUIO

solution was regulated to a range of 2–8 by adding negligible amounts of 0.1 M HCl and NaOH solutions. In the uranium adsorption experiment, 20 mg adsorbents were added into the 10 mg/L U(VI) solution. The mixture was shaken at 160 rpm in an air batch shaker. After continuous shaking to reach adsorption equilibrium, the adsorbent was separated from the reaction solution via centrifugation and filtration. The residual concentration of U(VI) in the supernatant was measured via a standard spectrophotometry method (578 nm). It was based on the formation of colored complexes of U(VI) ion with bromine generation ethanol in aqueous medium [23]. The average values of each experimental result were obtained through three repeated experiments. The % adsorption and adsorption capacity q (mg/g) were calculated by the following Eqs. (1) and (2):

$$\%\ \text{adsorption} = \frac{C_0 - C_e}{C_0} \times 100\% \tag{1}$$

$$q = \frac{(C_0 - C_e) \times V}{M} \tag{2}$$

where C_0 is the initial U(VI) concentration (mg/L), C_e is the equilibrium concentration (mg/L), V is the volume of the solution (L), M is the mass of the adsorbent (g).

Adsorption–desorption test

The 20 mg of CNUIO adsorbed by U(VI) was added to 50 mL HCl (0.1 M) and desorbed by shaking for 6 h. A certain volume of the supernatant was centrifuged at 7000 rpm for 10 min. The concentration of U(VI) was measured, and its desorption rate was calculated. Desorbed CNUIO was repeatedly washed with distilled water, dried by a vacuum drying tank, and repeatedly adsorbed five times under the same conditions to determine the adsorption efficiency. The % desorption was calculated by the following Eqs. (3):

$$\%\ \text{desorption} = \frac{q_0}{q} \times 100\% \tag{3}$$

where q_0 is the desorption capacity of U (VI) (mg/g), q is the adsorption capacity of U (VI) (mg/g).

Characterization

The morphology of the adsorbents was observed via scanning electron microscopy (SEM) (JSM–7500F, Japan). The surface area of the adsorbents was determined by Brunauer–Emmett–Teller (BET) analysis, and the pore size and volume were calculated by Barrett–Joyner–Halenda (BJH) model (Micro for Tristar II,USA). The crystal texture of the adsorbents was identified using an XRD (Bruker D8, Germany). The functional groups of the adsorbents were ascertained via Fourier transform infrared (FTIR) spectroscopy (Nicolet–iS10, USA). The chemical elements of the adsorbents were identified via X-ray photoelectron spectroscopy (XPS) (ESCALAB250Xi, USA).

Results and discussion

Experiments on adsorption performance of CNUIO

Effects of pH and ionic strength

The effect of the initial pH value (2–8) on U(VI) removal by the three adsorbents were evaluated (Fig. 1). When the pH value increased from 2 to 6, the adsorption rate of CNUIO for U(VI) increased from 22.03% to 95.01%. When the pH value increased to 8, the adsorption rate decreased to 88.90%. At pH 6, the adsorption rate of CNUIO for U(VI) was about 25% and 33.73% higher than that of g-C_3N_4 and UiO-66, respectively. Furthermore, the removal rate of U(VI) by g-C_3N_4 and UiO-66 was lower than that of CNUIO within the range of pH values studied herein, indicating that the adsorption performance of the composite on U(VI) was better than that of each single component.

The effects of pH may be attributed to the fact that the acid–base of the solution has an important effect on the morphology of uranium, the surface charge distribution of the adsorbent, and the binding sites. The uranyl ion species in natural water has been widely studied [24]. The reason for the changes in the adsorption rate of CNUIO to U(VI) with pH was further explored by simulating uranyl species at different pH values by using the Visual

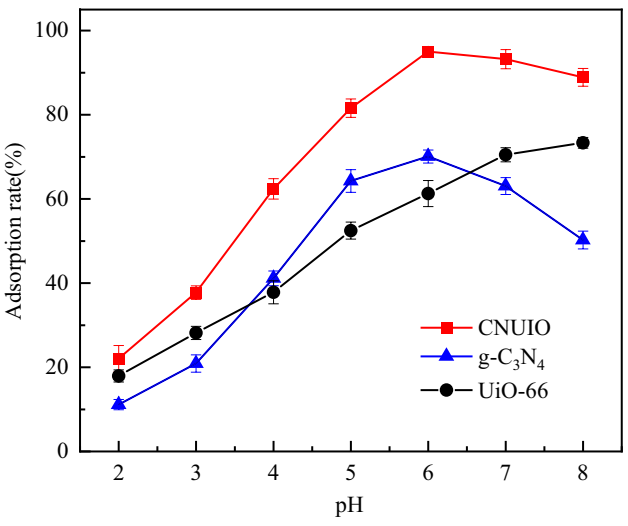

Fig. 1 The effect of the pH on U(VI) adsorption onto g-C_3N_4, UiO-66 and CNUIO. (M/V = 0.4 g/L, $C_{U(VI)}$ = 10 mg/L, T = 298 K, t = 120 min)

MINTEQ software. As shown in Fig. 2, at pH < 4, U(VI) mainly existed as UO_2^{2+}, and at pH = 5–7, several kinds of uranyl hydroxides, such as $UO_2(OH)^+$, $(UO_2)_3(OH)_5^+$ and $(UO_2)_4(OH)_7^+$, were gradually generated. When pH = 6, the dominating uranyl specie is $(UO_2)_3(OH)_5^+$ and the adsorption rate reached 95.01%. At pH > 8, the predominant species are $UO_2(CO_3)_3^{4-}$ and $UO_2(CO_3)_2^{2-}$.

According to the zeta potential (Fig. 3), the point of zero charge of CNUIO was measured at pH = 6.02. The surface of the adsorbent was positively charged prior to 6.02 because of the protonation of functional groups on CNUIO by H^+. At this time, electrostatic repulsion was formed between the protonated adsorbents and the positively charged UO_2^{2+}; moreover, the high concentration of H^+ completed with UO_2^{2+} for the active sites, thereby restricting uranium adsorption [25]. As pH increased, the surface charge of CNUIO changed from positive to negative. Owing to the electrostatic attraction between CNUIO and UO_2^{2+}, adsorption efficiency gradually improved. After the zero potential, the negatively charged CNUIO repelled each other with various U(VI) complexes, such as $UO_2(CO_3)_3^{4-}$ and $UO_2(CO_3)_2^{2-}$, resulting in a slight decrease in adsorption rate.

The influence of ionic strength on U(VI) adsorption by CNUIO was assessed (Fig. 4). When Na^+ concentration increased from 0 to 0.1 mol/L, U(VI) adsorption was negligibly affected within the specified pH range, indicating that the adsorption was dominated by inner-sphere surface complexation and electrostatic attraction [26].

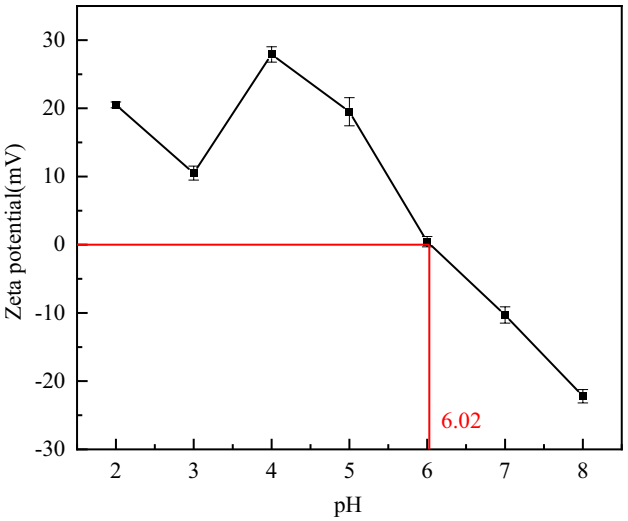

Fig. 3 The zeta potential changes with different pH

Effects of adsorbent dosages

The dosage of CNUIO may affect the number of binding sites between CNUIO and U(VI), thus affecting the adsorption capacity of U(VI). The effect of CNUIO dosages on U(VI) adsorption were examined (Fig. 5). When the dosage increased from 0.1 to 1.6 g/L, the adsorption efficiency of U(VI) by CNUIO increased from 69.19 to 97.4%, whereas the adsorption capacity decreased from 69.19 to 6.09 mg/g. As the dosage increased, the number of active sites of the adsorbents and the adsorption rate of U(VI) correspondingly increased [27]. However, excessive CNUIO dosages will reduce the unsaturation sites per unit mass adsorption, so the adsorption capacity was decreased. When CNUIO

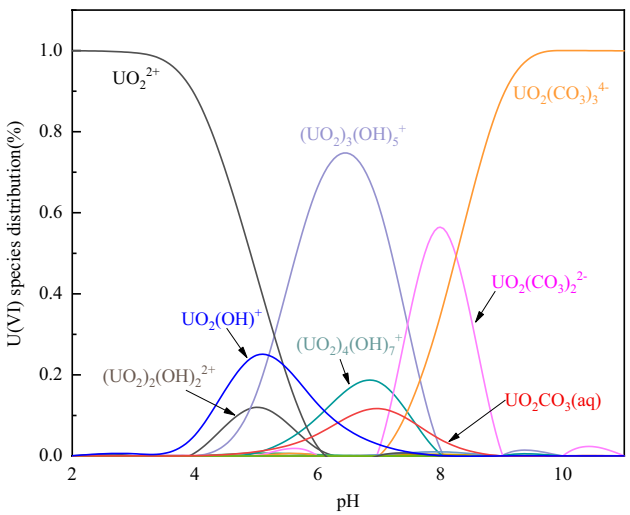

Fig. 2 The distribution of U(VI) species in aqueous solution with different pH

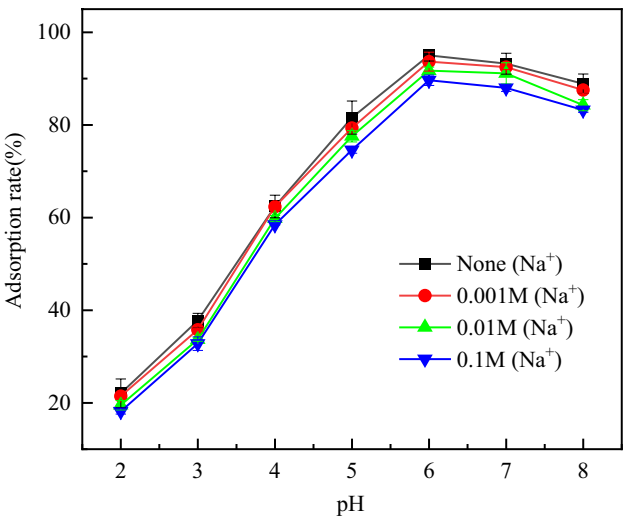

Fig. 4 The effect of ionic strength on U(VI) adsorption by CNUIO. (M/V = 0.4 g/L, $C_{U(VI)}$ = 10 mg/L, T = 298 K, t = 120 min)

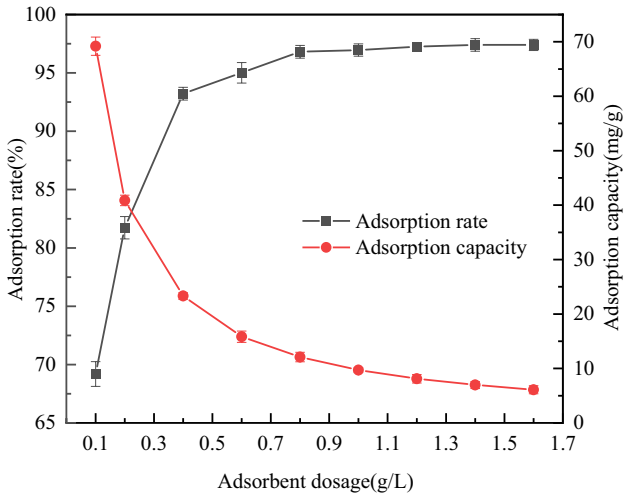

Fig. 5 Effect of the adsorbent dosage on U(VI) adsorption to CNUIO. (pH = 6, $C_{U(VI)}$ = 10 mg/L, T = 298 K, t = 120 min)

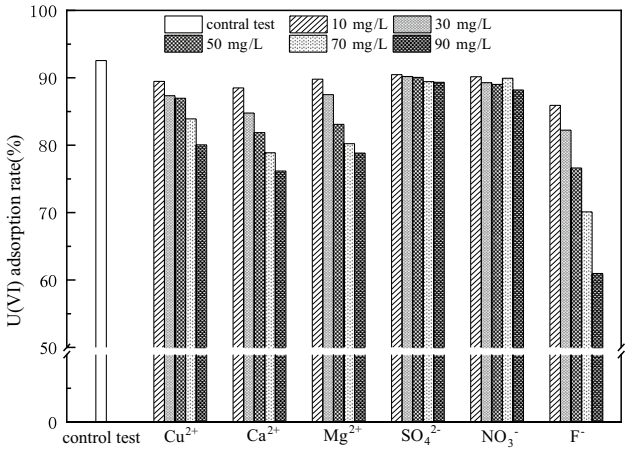

Fig. 6 Effects of coexisting-ions on U(VI) adsorption by CNUIO. (pH = 6, M/V = 0.4 g/L, $C_{U(VI)}$ = 10 mg/L, T = 298 K, t = 120 min)

dosage exceeded 0.4 g/L, U(VI) adsorption tended to remain stable. Therefore, the subsequent dosage of CNUIO in this experiment was 0.4 g/L.

Effects of coexisting ions

The effects of coexisting ions on U(VI) adsorption by CNUIO are illustrated in Fig. 6. A low concentration of the coexisting ions (10 mg/L) had little effect on CNUIO adsorption. As their concentration increased, SO_4^{2-} and NO_3^- had little effect on U(VI) adsorption. However, Cu^{2+}, Ca^{2+}, Mg^{2+}, and F^- inhibited the adsorption to a certain extent, and the degree of inhibition was positively correlated with the concentration of the coexisting ions. Cu^{2+}, Ca^{2+}, and Mg^{2+} competed with uranyl ions for CNUIO surface activity adsorption sites during the adsorption process, resulting in a decrease in adsorption rate. The adsorption inhibition of F^- on U(VI) was the strongest. When the concentration of F^- was 90 mg/L, the adsorption rate was only 60.97%. Owing to the high affinity between fluorine and zirconium, zirconium-based adsorbents usually exhibit ideal F^- removal [28]. Therefore, in the presence of interference ions other than F^-, the removal rate of U(VI) by CNUIO remained above 80%, indicating that CNUIO had a certain selective adsorption of U(VI) in aqueous solutions.

Effects of contact time and adsorption kinetics

The effect of contact time on adsorption of CNUIO was shown in Fig. 7(a). As can be seen, the adsorption capacity rapidly increased within the first 20 min, and the adsorption equilibrium was reached within 60 min. This result was attributed to the sufficient active sites on CNUIO and the large concentration gradient at the initial stage. As the adsorption progressed, the active sites on the CNUIO surface became saturated, resulting in almost no increase in adsorption capacity.

The adsorption behavior of U(VI) was simulated by the pseudo-first-order model (Eq. (4)), pseudo-second-order model (Eq. (5)), and intraparticle diffusion model (Eq. (6)):

$$\ln(q_e - q_t) = \ln q_e - k_1 t \tag{4}$$

$$\frac{t}{q_t} = \frac{1}{k_2 \cdot q_e^2} + \frac{t}{q_e} \tag{5}$$

$$q_t = k_i \cdot t^{\frac{1}{2}} + C \tag{6}$$

where q_e is the equilibrium adsorption capacity (mg/g), and q_t (mg/g) is the adsorption capacity at time t (min). k_1 (min^{-1}), k_2 (min^{-1}), and k_i ($mg/m{\cdot}min^{1/2}$) are the adsorption rate constants of the pseudo-first, pseudo-second, and intraparticle diffusion models, respectively.

The dynamic model fitting curves are plotted in Fig. 7(b)–(d), and the fitting parameters were listed in Table 1. The equilibrium adsorption capacity fitted in the pseudo-second-order kinetic model was closer to the U(VI) adsorption capacity obtained from the test, and the correlation coefficient (R^2 = 0.999) was high, indicating that the pseudo-second-order kinetic model could describe the adsorption process better. Thus, the adsorption was mainly based on the chemical adsorption [29]. In addition, as intercept not zero, intraparticle diffusion is not the only rate limiting step.

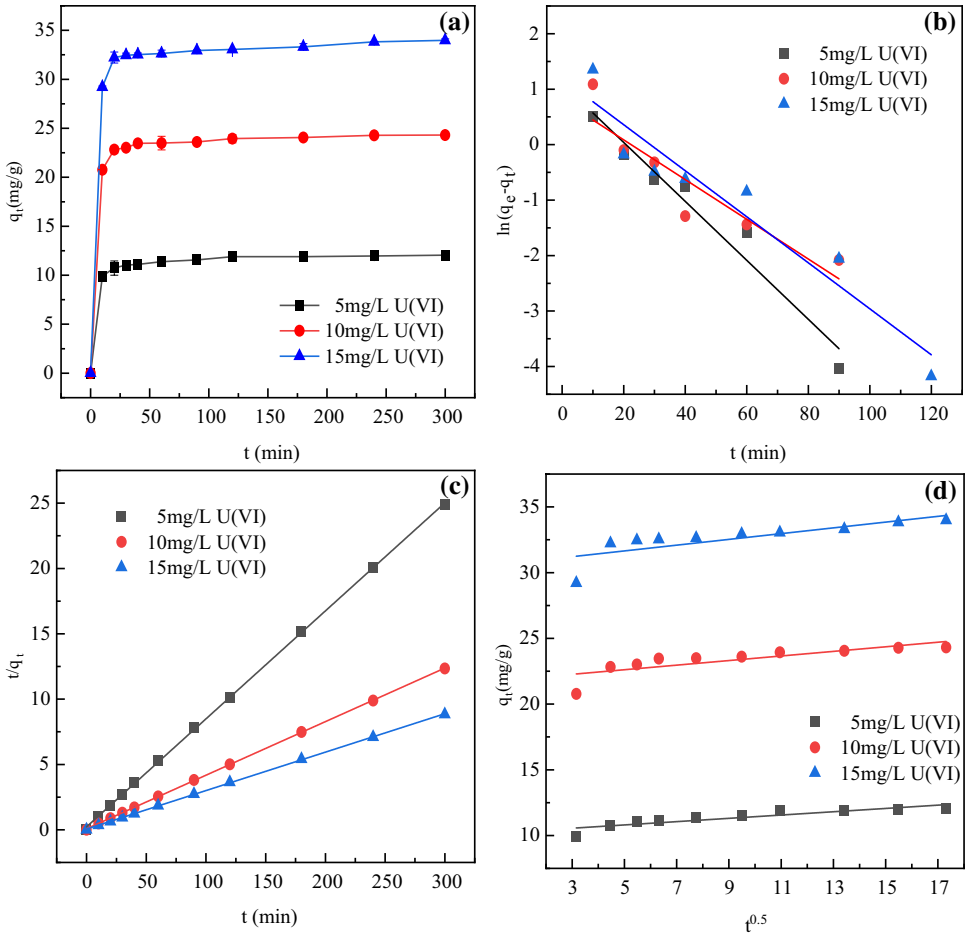

Fig. 7 Effect of contact time on U(VI) adsorption by CNUIO (**a**), pseudo-first-order model (**b**); pseudo-second-order model (**c**), intra-particle-diffusion model (**d**). (pH = 6, M/V = 0.4 g/L, $C_{U(VI)}$ = 10 mg/L, T = 298 K)

Table 1 Adsorption dynamics model of U(VI) on CNUIO

C_0/(mg/L)	$q_{e,exp}$/(mg/g)	Pseudo-first-order			Pseudo-second-order			Intra-particle-diffusion		
		k_1	$q_{e,cal}$	R^2	k_2	$q_{e,cal}$	R^2	C	k_i	R^2
5	12.04	0.182	11.57	0.950	0.037	11.97	0.999	10.17	0.125	0.779
10	24.31	0.203	23.73	0.805	0.025	24.31	0.999	21.74	0.174	0.608
15	33.98	0.212	33.06	0.904	0.021	33.76	0.999	30.55	0.219	0.584

Adsorption isotherms and thermodynamic analysis

To further explore the adsorption behavior, the experimental data were fitted by the Langmuir model (Eq. (7)) and Freundlich isotherm model (Eq. (8)).

$$\frac{C_e}{q_e} = \frac{1}{b \cdot q_{max}} + \frac{C_e}{q_{max}} \tag{7}$$

$$\ln q_e = \ln k_F + \frac{1}{n} \ln C_e \tag{8}$$

where C_e is the concentration of U(VI) after adsorption equilibrium (mg/L), b is Langmuir adsorption equilibrium constant (L/mg), q_{max} is the maximum adsorption capacity (mg/g), k_F is the Freundlich adsorption equilibrium constant, and n is a dimensionless constant.

The fitting curves were shown in Fig. 8, and more fitted parameters were provided in Table 2. A comparison of the correlation coefficient between the two models revealed that the process of U(VI) adsorption on CNUIO was more consistent with the Langmuir model. The adsorption process was a uniform monolayer adsorption, and the interaction between adjacent uranyl ions could be ignored. The separation factor R_L ($R_L = 1/(1 + bC_0)$) [30] in the Langmuir model was 0.423, 0.510 and 0.609 in the range of (0–1), thereby demonstrating that the adsorption of U(VI) by CNUIO was favorable. Furthermore, the maximum adsorption capacity was calculated from the Langmuir model was 261.16 mg/g. The comparison of adsorption

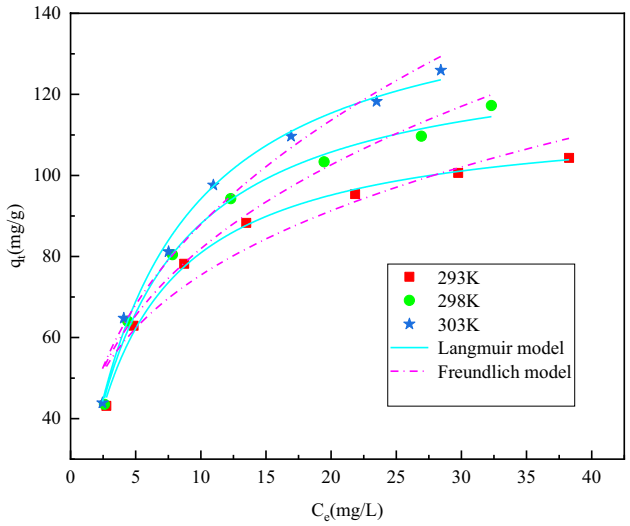

Fig. 8 The fitting of adsorption isotherm model. (pH = 6, M/V = 0.4 g/L, t = 60 min)

$$\ln K^0 = \frac{\Delta S^0}{R} - \frac{\Delta H^0}{RT} \quad (9)$$

$$\Delta G^0 = -RT \cdot \ln K^0 \quad (10)$$

where K^0 is the distribution coefficient, R is the universal gas constant (8.312 J mol^{-1} K^{-1}), T is the temperature (K). The thermodynamic parameters for the adsorption of U(VI) on CNUIO were listed in Table 4. The values of ΔH^0 and ΔS^0 were determined from the intercept and slope of lnK^0 and 1/T linear curve (Fig. 9), and the value of ΔG^0 at the three temperature was calculated according to the above formula.

$\Delta G^0 < 0$ and $\Delta H^0 > 0$ confirmed that the adsorption was a spontaneous endothermic process. $\Delta S^0 > 0$ indicated an increase in disorder throughout adsorption. Meanwhile, the value of ΔG^0 decreased as temperature increased. This result indicated that the rise in temperature was conducive to the adsorption of U(VI) on CNUIO because this phenomenon can provide more energy for the reaction

Table 2 Parameters of Langmuir and Freundlich model of U(VI) at 293, 303, 313 K

T/K	Langmuir			Freundlich		
	q_{max}	b	R^2	k_F	n	R^2
293	225.34	0.017	0.996	5.552	1.384	0.967
298	235.42	0.012	0.994	7.080	1.542	0.949
303	261.16	0.008	0.994	9.184	1.770	0.920

Table 3 Comparison of the capacities with other adsorbents for U(VI)

Adsorbents	Conditions	q_{max}/(mg g^{-1})	References
CNUIO	pH = 6, T = 303 K	261.16	This study
PCN	pH = 5, T = 303 K	92	[13]
g-C_3N_4@Ni-Mg–Al-LDH	pH = 5, T = 298 K	99.70	[31]
PPy/g-C_3N_4	pH = 5, T = 298 K	196.08	[32]
UiO-66-TBP	pH = 5, T = 298 K	201.9	[33]
UiO-66-AO	pH = 5.5, T = 313 K	227.80	[34]
GO-COOH/UiO-66	pH = 8, T = 298 K	188.30	[35]

capacities of various uranium adsorbents was provided in Table 3. CNUIO exhibited superior adsorption performance, which verified its great potential in the field of uranium-containing water treatment.

In order to better reflect the feasibility of the adsorption process, the thermodynamic parameters entropy change (ΔS^0), the enthalpy change (ΔH^0), and the standard free energy charge(ΔG^0) were calculated according to the following Eqs. (9) and (10).

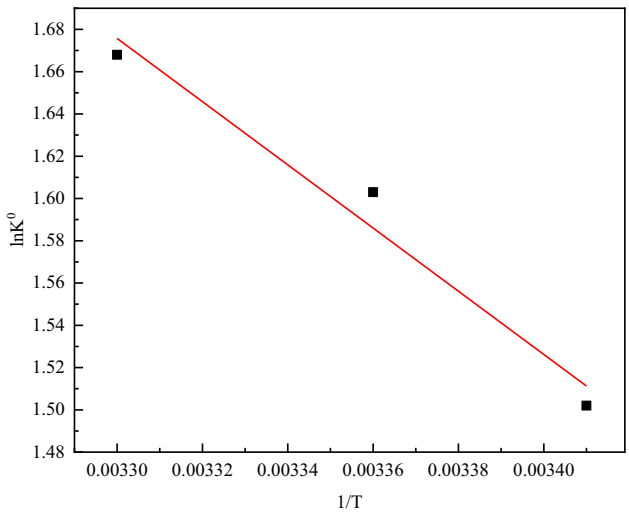

Fig. 9 The plots of lnK^0 versus 1/T for U(VI) adsorption on CNUIO

Table 4 CNUIO absorbs the thermodynamic parameters of U(VI)

ΔG^0/ (KJ mol^{-1})			ΔH^0/ (KJ mol^{-1})	ΔS^0/(J mol^{-1})
293 K	298 K	303 K	12.43	54.94
−3.66	−3.97	−4.20		

process and promote the formation of stable chemical bonds between the surface of adsorbent and uranyl ions, thereby promoting the adsorption [36].

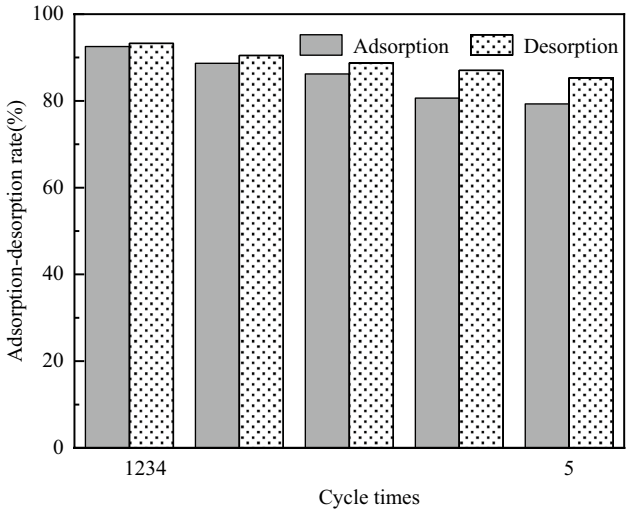

Fig. 10 The effect of cycle times on U(VI) adsorption–desorption by CNUIO. (pH = 6, M/V = 0.4 g/L, $C_{U(VI)}$ = 10 mg/L, T = 298 K)

Adsorption–desorption experiment of CNUIO

The five adsorption–desorption cycles of CNUIO using 0.1 mol/L HCl are shown in Fig. 10. The initial adsorption rate and desorption rate of CNUIO were 92.55% and 93.27%, respectively. In the first three experiments, the effective removal of U(VI) could still be maintained (removal rate > 85%). When the desorption experiment was repeated five times, the adsorption rate decreased to about 80% probably because some adsorption sites on the material surface were not successfully desorbed during the desorption process. In the process of acid desorption, part of H^+ occupied the surface binding site. Although the desorbed adsorbent was washed to neutral several times before the next cycle, the effect of acid treatment was irreversible, resulting in the gradual reduction in removal rate. The five adsorption–desorption tests demonstrated that CNUIO had a strong renewable capacity within a short time, and multiple cycles reduced its adsorption capacity.

Characterization of the adsorbents

SEM–EDS analysis

The SEM images of g-C_3N_4, UiO-66, and CNUIO are given in Fig. 11. g-C_3N_4 was composed of dense, thick-layered block structures, and its surface was relatively smooth

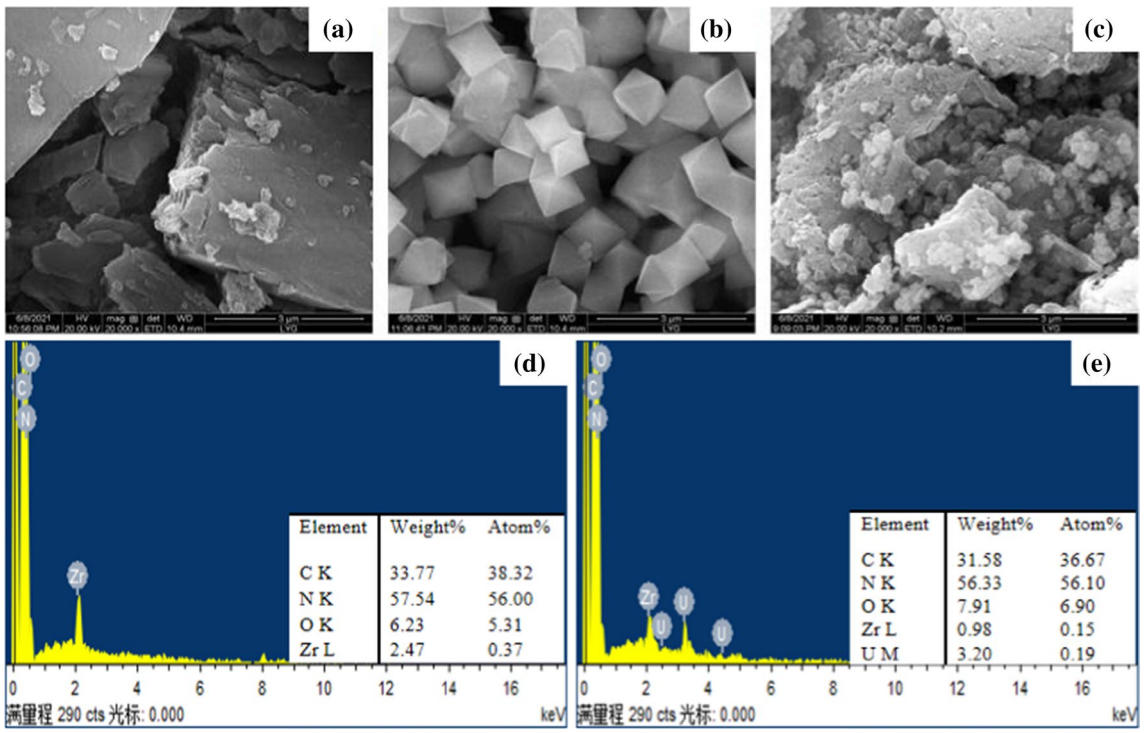

Fig. 11 SEM images of g-C_3N_4 (**a**), UiO-66 (**b**), CNUIO (**c**), EDS patterns of CNUIO adsorption U(VI) before(**d**), after (**e**)

(Fig. 11(a)). UiO-66 had an obvious cubic structure with a smooth surface and a uniform particle size (Fig. 11(b)). CNUIO had a rougher and more wrinkled structure than g-C_3N_4 (Fig. 11(c)). Moreover, g-C_3N_4 had a small particle aggregation, indicating that UiO-66 nanoparticles were successfully loaded on the g-C_3N_4 layer, and a small amount was intercalated between g-C_3N_4 layers. After the introduction of UiO-66, the thickness of block g-C_3N_4 became thin, which greatly increased its specific surface area and promoted U(VI) adsorption.

The EDS elemental energy spectra of CNUIO before and after U(VI) adsorption are shown in Figs. 11(d) and (e). The elemental composition of CNUIO before absorption mainly consisted of O, C, N, and Zr (Fig. 11(d)). The abundant O and N elements formed oxygen-containing and nitrogen-containing functional groups, thereby providing numerous active sites for U(VI) adsorption. The increase in uranium peak in the Fig. 11(e) proved that U(VI) was successfully adsorbed onto the sample surface. The drastic decrease in weight (%) of Zr after U(VI) adsorption may be the interaction between the Zr–O bond and U(VI).

XRD analysis

The crystal structure of g-C_3N_4 and CNUIO are characterized via XRD. Figure 12 shows two characteristic peaks at 13.1° and 27.4° in g-C_3N_4, corresponding to planar packing of tri-s-triazine units are the (100) peak and interlayer stacking of conjugated aromatic system as the (002) peak, respectively [37]. The decrease of the (002) peak value in CNUIO indicated that the graphite layer spacing became larger, further confirming the intercalation phenomenon of UiO-66.

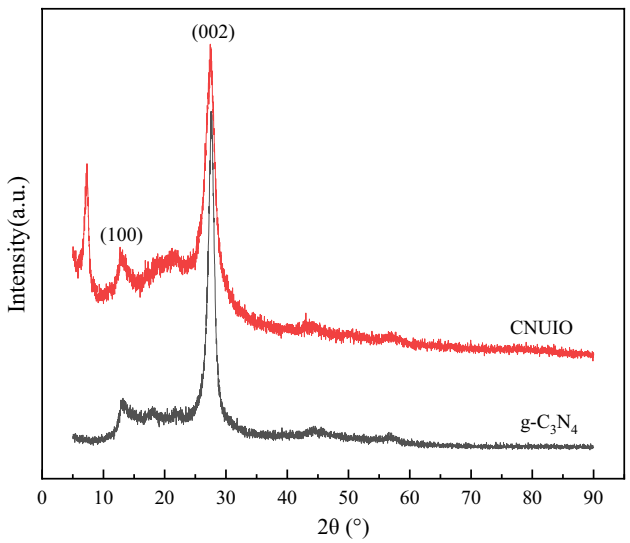

Fig. 12 XRD patterns of g-C_3N_4 and CNUIO

BET analysis

The N_2 adsorption–desorption isotherms of g-C_3N_4 and CNUIO are shown in Fig. 13. The text parameters are summarized in Table 5. The adsorption curves of CNUIO were similar to those of the typical type IV isotherm with obvious H3 hysteresis loops, indicating the presence of mesopores in the materials [38]. The smaller pore size of the composite indicated that UiO-66 particles stay in the channel of g-C_3N_4, resulting in the increase of specific surface area from 5.92 to 40.03 m^2/g. The incorporation of UiO-66 substantially enlarged the specific surface area and the pore volume of g-C_3N_4, further confirming that the excellent adsorption performance of CNUIO could be attributed to its large specific surface area.

Mechanisms of U(VI) adsorption on CNUIO

FT-IR spectroscopy

The FT-IR spectra of CNUIO before and after adsorption only slightly changed (Fig. 14), indicating that the structure and surface functional groups of CNUIO were not destroyed during the adsorption process. This result also indicated that the material had good regeneration properties. After U(VI)

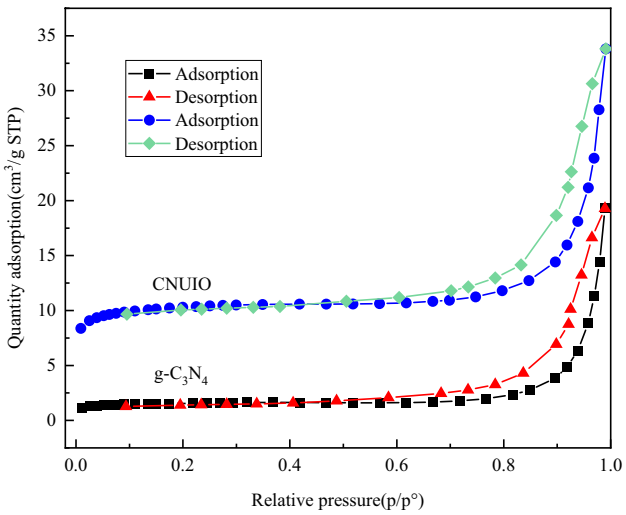

Fig. 13 N_2 adsorption–desorption isotherms of g-C_3N_4 and CNUIO

Table 5 BET surface area and pore parameters of the g-C_3N_4 and CNUIO

Sample	S_{BET} (m^2/g)	Pore volume (cm^3/g)	Pore size (nm)
g-C_3N_4	5.92	0.029	20.17
CNUIO	40.03	0.052	5.22

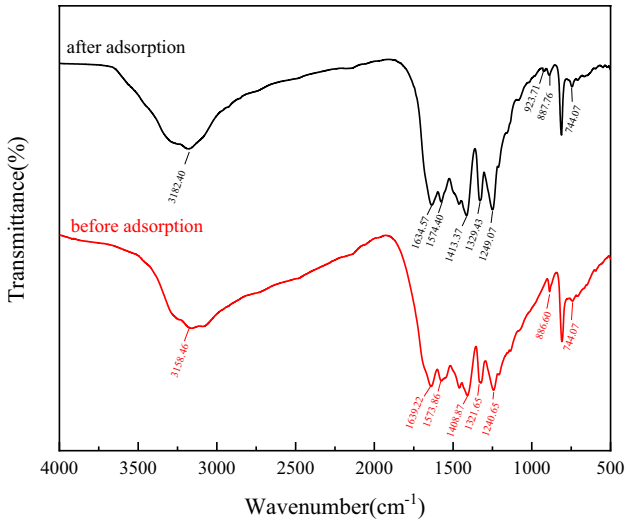

Fig. 14 FT-IR spectra before and after CNUIO adsorption U(VI)

adsorption, some of the peaks showed the changes of displacement and strength. The increase in the band strength at 923.71 cm^{-1} was attributed to the O = U = O stretching vibration [39]. The main peak shifted, the broad peak at 3000–3500 cm^{-1} was associated with the stretching vibration of N–H and –OH, resulting from uncondensed amino groups (–NH_2– or –NH–) and absorbed water. However, the shape and strength of the peak did not remarkably change, which might have been caused by the complexation between N–H and –OH and U(VI) [40]. Several typical vibrations of carbon–nitrogen heterocycles were detected within the 1200–1700 cm^{-1} wavenumber range. The C = N tensile vibration peaks at 1639.22 and 1573.86 cm^{-1} shifted to 1634.57 and 1574.40 cm^{-1}, respectively [41]. The C–N tensile vibration peaks at 1408.87, 1321.65, and 1240.65 cm^{-1} moved to 1413.37, 1329.43, and 1249.07 cm^{-1}, respectively [42]. The N–H stretching vibration peak at 886.60 cm^{-1} caused by incomplete condensation of amino moved to 887.76 cm^{-1} [43]. These movements may be the formation of complexes between nitrogen-containing functional groups and U(VI) in CNUIO. Furthermore, the Zr–O bond (744.07 cm^{-1}) peak position did not change, but the vibration peak intensity increased, which indicated that Zr–O was also involved in the reaction [44]. On the basis of the changes in FTIR spectra before and after adsorption, N–H, –OH, C = N, C–N and Zr–O are speculated to be the main adsorption sites in the process of U(VI) adsorption by CNUIO.

XPS analysis

The interaction mechanism between CNUIO and U(VI) was further analyzed via XPS (Fig. 15). The total spectrum of the sample indicated that the element types contained in the material were consistent with the EDS results (Fig. 15(a)). The two peaks at the binding energy of 392.70 and 381.93 eV were attributed to U4f $_{5/2}$ and U4f $_{7/2}$ peaks in hexavalent form, respectively (Fig. 15(b)), illustrating that U(VI) was only adsorbed onto the CNUIO surface via oxidation [45].

The typical Zr3d $_{3/2}$ and Zr3d $_{5/2}$ peaks at 185.24 and 182.85 eV revealed the existence of Zr^{4+} (Fig. 15(c)) [46]. After adsorption, the two peaks moved to the low binding energy end probably because of the interaction between the Zr–O bond and U(VI) [47]. The high-resolution spectrum of C1s is shown in Fig. 15(d). The peak at 284.80 eV came from the graphitic carbon or the amorphous carbon of the sp^2 C–C bond in g-C_3N_4, whereas the peak at 288.19 eV was the sp^2 hybridized carbon (N–C = N) in the triazine ring structure that was bound to nitrogen atom [48]. The weak peak at 286.01 eV was attributed to the C–NH_x ($x = 1, 2$) groups at the edge of heptazine [49]. The pre-adsorption N1s spectra at 404.64, 400.42, and 398.63 eV belonged to N–oxide [50], the N–H bond, and the C–N = C sp^2 hybrid nitrogen, respectively (Fig. 15(e)) [51]. The binding energy of the three peaks increased after adsorption because the lone pair of electron in the N atom transferred to the unoccupied orbital of U electron, resulting in a decrease in electron cloud density and the positive movement of binding energy [52]. Additionally, the decrease of diffraction peak intensity can be attributed to the combination of these functional groups with U(VI), which is consistent with the FTIR results. In the spectrum of O1s, the peak at 532.30 eV corresponded to the surface hydroxyl group of melamine thermal polymerization [53], whereas the peaks at 531.65 and 530.15 eV represented the C = O and Zr–O bonds, respectively (Fig. 15(f)) [54]. After U(VI) adsorption, the binding of O1s peaks shifted to higher, thereby demonstrating that the oxygen-containing functional groups on the surface of CNUIO provided active sites for U(VI) adsorption. To sum up, the above results demonstrated that the nitrogen- and oxygen-containing functional groups were in charge of the interaction between CNUIO and U(VI).

Conclusion

In this work, CNUIO was synthesized and successfully applied to U(VI) adsorption. Tests demonstrated that this composite had good reusability. Under the conditions of pH 6, absorbent dosage = 0.4 g/L, $t = 120$ min, and $C_{U(VI)} = 10$ mg/L, the adsorption rate of U(VI) by CNUIO was 95.01%. U(VI) adsorption onto CNUIO was strongly dependent on pH but independent of ionic strength, indicating that the adsorption process was dominated by inner-sphere surface complexation and electrostatic attraction. The adsorption process fitted well with

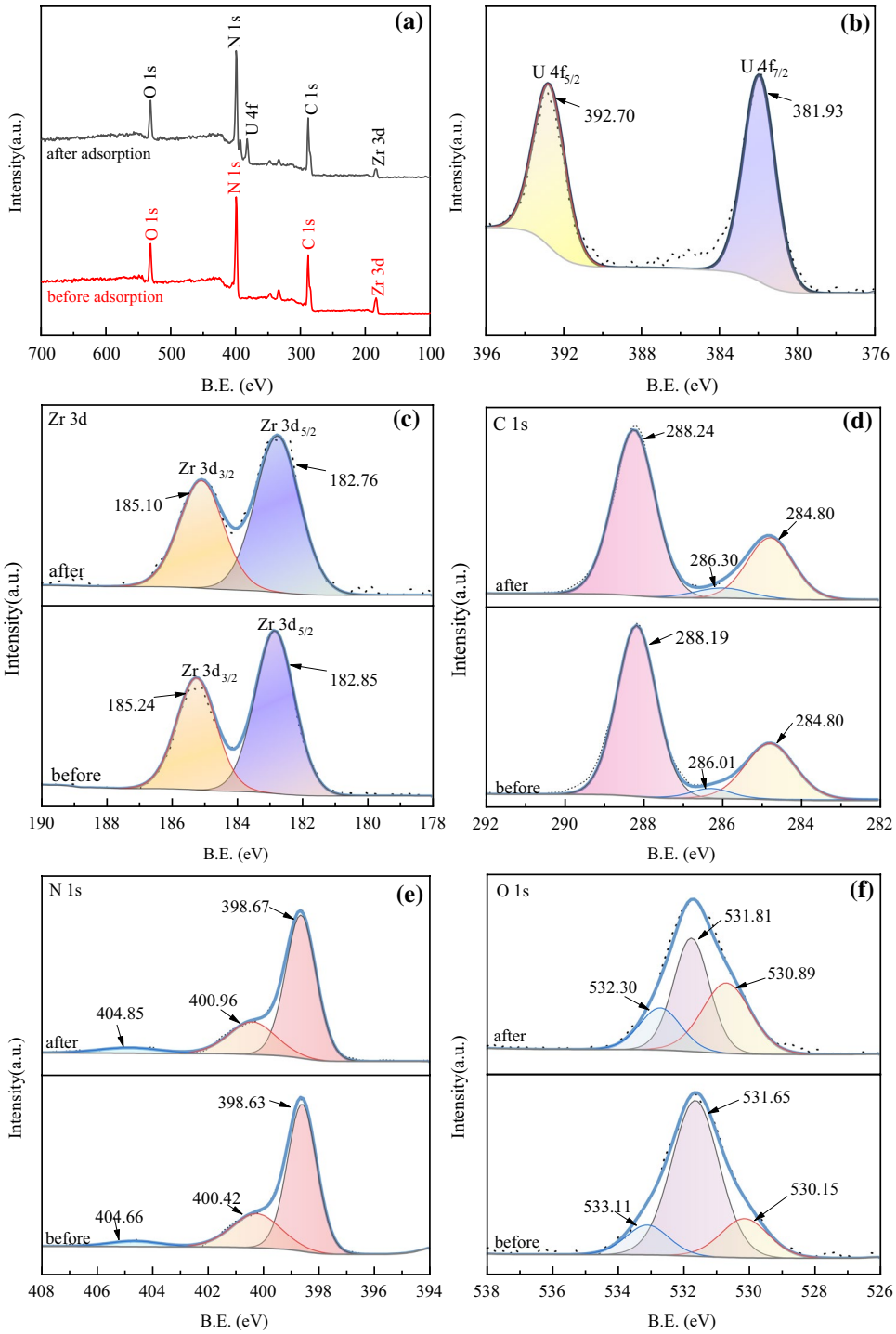

Fig. 15 XPS survey spectra for CNUIO before and after U(VI) adsorption (**a**), the corresponding high-resolution spectra of U4f (**b**), Zr3d (**c**), C1s (**d**), N1s (**e**), O1s (**f**)

the pseudo-second-order kinetic model and the Langmuir isothermal adsorption model, indicating that U(VI) adsorption was mainly monolayer chemical adsorption on the CNUIO surface. The maximum Langmuir adsorption capacity was 261.16 mg/g. Thermodynamic parameters ($\Delta G^0 < 0$ and $\Delta H^0 = 12.427$ kJ mol^{-1}) revealed that U(VI) adsorption by CNUIO was a spontaneous endothermic process. SEM–EDS and BET analysis revealed that the specific surface area of CNUIO substantially increased, which promoted U(VI) adsorption. According to the results of FTIR spectroscopy and XPS, the underlying adsorption mechanism was the synergistic complexation of nitrogen-containing and oxygen-containing functional groups. In conclusion, CNUIO can be used as a suitable adsorbent in practical radioactive wastewater treatment.

Acknowledgements This work was supported by the National Natural Science Foundation of China [Grant Numbers NO42177074].

Declarations

Conflict of interest The authors declare that they have no known competing financial interests or personal relationships that could have appeared to influence the work reported in this paper. The authors declare the following financial interests/personal relationships which may be considered as potential competing interests.

References

1. Gudkov SV, Chernikov AV, Bruskov V (2016) Chemical and radiological toxicity of uranium compounds. Russ J Gen Chem 86(6):1531–1538
2. Li ZJ, Huang ZW, Guo WL et al (2017) Enhanced photocatalytic removal of uranium(VI) from aqueous solution by magnetic TiO_2/Fe_3O_4 and Its graphene composite. Environ Sci Technol 51(10):5666–5674
3. Sarafraz H, Minuchehr A, Alahyarizadeh G et al (2017) Synthesis of enhanced phosphonic functional groups mesoporous silica for uranium selective adsorption from aqueous solutions. Sci Rep-UK 7(1):11675
4. Orrego P, Hernández J, Reyes A (2019) Uranium and molybdenum recovery from copper leaching solutions using ion exchange. Hydrometallurgy 184:116–122
5. Ling L, Zhang W (2015) Enrichment and encapsulation of uranium with iron nanoparticle. J Am Chem Soc 137(8):2788–2791
6. Dai ZG, Zhen Y, Sun YS et al (2021) ZnFe2O4/g-C3N4 S-scheme photocatalyst with enhanced adsorption and photocatalytic activity for uranium (VI) removal. Chem Eng J 415:129002
7. Taxakoli HZ, Abdollahym M, Ahmadi SJ et al (2017) Enhancing recovery of uranium column bioleaching by process optimization and kinetic modeling. T Nonferr Metal Soc 27(12):2691–2703
8. Yan T, Jiang F, Chen H (2014) Adsorptive removal of perfluorooctane sulfonate from water by mesoporous carbon nitride. Acta Sci Circum 34(6):1464–1472
9. Dong XP, Cheng F (2015) Recent development in exfoliated two-dimensional g-C_3N_4 nanosheets for photocatalytic applications. J Mater Chem A 3(47):23642–23652
10. Liu JX, Chen ZG, Xie SB et al (2019) Adsorption properties and mechanism of U(VI) onto mxidized graphitic carbon nitride nanomaterials. Fine Chem 36(7):1–10
11. Shen CC, Chen CL, Wen T et al (2015) Superior adsorption capacity of g-C_3N_4 for heavy metal ions from aqueous solutions. J Colloid Interface Sci 456:7–14
12. Nguyen TKA, Pham TT, Huy NP et al (2021) The effect of graphitic carbon nitride precursors on the photocatalytic dye degradation of water-dispersible graphitic carbon nitride photocatalysts. Appl Surf Sci 537:148027
13. Ge YJ, Wu J, Wang GH et al (2021) Preparation of porous graphite phase carbon nitride ang its adsorption property for U(VI). Atomic Energy Sci Technol 55(4):603–611
14. Liu JX, Chen ZG, Yu K et al (2019) Polyaniline/oxidation etching graphitic carbon nitride composites for U(VI) removal from aqueous solutions. J Radioanal Nucl Chem 321(3):1005–1017
15. Ge YJ, He ZQ, Wu J et al (2020) Manganese ferrite/porous graphite carbon nitride composites for U(VI) adsorption from aqueous solutions. J Radioanal Nucl Chem 326(1):157–171
16. Long W, Liu HJ, Yan XM et al (2018) Preparation of new nano magnetic material Fe_3O_4@g-C_3N_4 and good adsorption performance on uranium ion. Mater Sci Eng 322:1–6
17. Hao X, Chen RR, Liu Q et al (2018) A novel U(VI)-imprinted graphitic carbon nitride composite for the selective and efficient removal of U(VI) from simulated seawater. Inorg Chem Front 5(9):2218–2226
18. Zhang Y, Zhou JB, Feng QQ et al (2018) Visible light photocatalytic degradation of MB using UiO-66/g-C_3N_4 heterojunction nanocatalyst. Chemosphere 212:523–532
19. Luo BC, Yuan LY, Tang Q (2015) U(VI) capture from aqueous solution by highly porous and stable MOFs: UiO-66 and its amine derivative. J Radioanal Nucl Chem 307(1):269–276
20. Du ZY, Li BL, Jiang C et al (2021) Sorption of U(VI) on schiff-base functionalized metal–organic frameworks UiO-66-NH_2. J Radioanal Nucl Chem 327(2):811–819
21. Tripathi S, Sreenivasulu B, Suresh A et al (2020) Assorted functionality-appended UiO-66-NH_2 for highly efficient uranium(VI) sorption at acidic/neutral/basic pH. RSC Adv 10(25):14650–14661
22. Zhang XD, Yang Y, Huang WY et al (2018) g-C_3N_4/UiO-66 nanohybrids with enhanced photocatalytic activities for the oxidation of dye under visible light irradiation. Mater Res Bull 99:349–358
23. Fan BY (1987) Spectrophotometric determination of trace uranium and thorium in environmental samples. Radiat Protect Bull 06:18–25
24. Cumberland SA, Douglas G, Grice K et al (2016) Uranium mobility in organic matter-rich sediments: A review of geological and geochemical processes. Earth-Sci Rev 159:160–185
25. Schierz A, Zanker H (2009) Aqueous suspensions of carbon nanotubes: surface oxidation, colloidal stability and uranium sorption. Environ Pollut 157(4):1088–1094
26. Sun YB, Yang SB, Chen Y (2015) Adsorption and desorption of U(VI) on functionalized graphene oxides: a combined experimental and theoretical study. Environ Sci Technol 49(7):4255–4262
27. Yao W, Wu YH, Pang HW et al (2018) In-situ reduction synthesis of manganese dioxide@polypyrrole core/shell nanomaterial for highly efficient enrichment of U(VI) and Eu(III). Sci China Chem 61(7):812–823
28. Xu RM, Ji QH, Zhao P et al (2020) Hierarchically porous UiO-66 with tunable mesopores and oxygen vacancies for enhanced arsenic removal. J Mater Chem A 8(16):7870–7879
29. Gu WY, Huang XY, Tian YH et al (2021) High-efficiency adsorption of tetracycline by cooperation of carbon and iron in a magnetic Fe/porous carbon hybrid with effective Fenton regeneration. Appl Surf Sci 538:147813
30. Wu P, Wang Y, Hu X (2018) Uranium adsorption on ferroferric oxide/graphene oxide nanoribbon composite material. Atom Energy Sci Technol 52(9):1561–1568
31. Zou YD, Wang PY, Yao W et al (2017) Synergistic immobilization of UO_2^{2+} by novel graphitic carbon nitride @ layered double hydroxide nanocomposites from wastewater. Chem Eng J 330:573–584
32. Yu K, Liu JX, Xie SB et al (2020) Study on the properties and mechanism of U(VI) adsorption of PPy/g-C_3N_4. Materials Rep 34(23):23020–23026
33. Rajaei A, Ghani K, Jafari M (2021) Modification of UiO-66 for removal of uranyl ion from aqueous solution by immobilization of tributyl phosphate. J Chem Sci. https://doi.org/10.1007/s12039-020-01864-4
34. Liu JM, Yin XH, Liu T (2019) Amidoxime-functionalized metal-organic frameworks UiO-66 for U(VI) adsorption from aqueous solution. J Taiwan Inst Chem E 95:416–423
35. Yang PP, Liu Q, Liu JY et al (2017) Interfacial growth of a metal–organic framework (UiO-66) on functionalized graphene oxide (GO) as a suitable seawater adsorbent for extraction of uranium(VI). J Mater Chem A 5(34):17933–17942

36. Feng S, Wang RB, Zhang ZH et al (2018) Synthesis and adsorption property of UiO-66/GO nanocomposites. Fine Chem 35(11):1942–1947
37. Yu HG, Ma HQ, Wu XH et al (2020) One-step realization of crystallization and cyano-group generation for g-C_3N_4 photocatalysts with Improved H_2 production. Solar RRL 5(2):2000372
38. Sing KSW, Everett DH, Haul RAW et al (1985) Reporting physisorption data for gas/solid systems with special reference to the determination of surface area and porosity. Pure Appl Chem 57(4):603–619
39. Muller K, Brendler V, Foerstendorf H (2008) Aqueous uranium(VI) hydrolysis species characterized by attenuated total reflection fourier-transform infrared spectroscopy. Inorg Chem 47(21):10127–10134
40. Zhang YC, Zhang Q, Shi QW et al (2015) Acid-treated g-C_3N_4 with improved photocatalytic performance in the reduction of aqueous Cr(VI) under visible-light. Sep Purif Technol 142:251–257
41. Zhang YJ, Thomas A, Antonietti M et al (2009) Activation of carbon nitride solids by protonation: morphology changes, rnhanced Ionic conductivity, and photoconduction experiments. Nat Mater 8(1):76–80
42. Pham TT, Shin E (2018) Influence of g-C_3N_4 precursors in g-C_3N_4/$NiTiO_3$ composites on photocatalytic behavior and the interconnection between g-C_3N_4 and $NiTiO_3$. Langmuir 34(44):13144–13154
43. Dong F, Wang ZY, Sun YJ et al (2013) Engineering the nanoarchitecture and texture of polymeric carbon nitride semiconductor for enhanced visible light photocatalytic activity. J Colloid Interf Sci 401:70–79
44. Rong LS, Xia L, Zhou SK et al (2021) Preparation of UiO-66/chitosan and its adsorption mechanism of U(VI). Acta Materiae Compositae Sinica 002:1–11
45. Liu Y, Yang YY, Chen L et al (2016) Efficient removal of U(VI) from aqueous solutions by polyaniline/hydrogen-titanate nanobelt composites. RSC ADV 6(61):56139–56148
46. Fan GD, Zhan JJ, Luo J et al (2019) Decorating Ag/AgCl on UiO-66-NH_2: synergy between Ag plasmons and heterostructure for the realization of efficient visible light photocatalysis. Chinese J Catal 40(8):1187–1201
47. Shokouhfar N, Aboutorabi L, Morsali A (2018) Improving the capability of UiO-66 for Cr(VI) adsorption from aqueous solutions by introducing isonicotinate N-oxide as the functional group. Dalton T 47(41):14549–14555
48. Yu CF, Tan L, Shen SJ et al (2021) In situ preparation of g-C_3N_4/polyaniline hybrid composites with enhanced visible-light photocatalytic performance. J Environ Sci 104(6):317–325
49. Li B, Zhang J, Luo ZY et al (2021) Amorphous B-doped graphitic carbon nitride quantum dots with high photoluminescence quantum yield of near 90% and their sensitive detection of Fe^{2+}/Cd^{2+}. Sci China Mater 64:1–14
50. Wang XL, Li GR, Li MJ et al (2021) Reinforced polysulfide barrier by g-C_3N_4/CNT composite towards superior lithium-sulfur batteries. J Energy Chem 53:234–240
51. Xie Y, Chen CL, Ren XM et al (2019) Coupling g-C_3N_4 nanosheets with metal-organic frameworks as 2D/3D composite for the synergetic removal of uranyl ions from aqueous solution. J Colloid Interf Sci 550:117–127
52. Guo DX, Song XM, Zhang LL et al (2020) Recovery of uranium (VI) from aqueous solutions by the polyethyleneimine-functionalized reduced graphene oxide/molybdenum disulfide composition aerogels. J Taiwan Inst Chem E 106:198–205
53. Zhang YZ, Chen ZW, Li JL et al (2021) Self-assembled synthesis of oxygen-doped g-C_3N_4 nanotubes in enhancement of visible-light photocatalytic hydrogen. J Energy Chem 54:36–44
54. Yang F, Xie SB, Wang GH et al (2020) Investigation of a modified metal-organic framework UiO-66 with nanoscale zero-valent iron for removal of uranium (VI) from aqueous solution. Environ Sci Pollut R 27(16):20246–20258